# Iron oxide nanoparticles fabricated by electric explosion of wire: focus on magnetic nanofluids

I. V. Beketov, A. P. Safronov, A. I. Medvedev, et al.

## ARTICLES YOU MAY BE INTERESTED IN

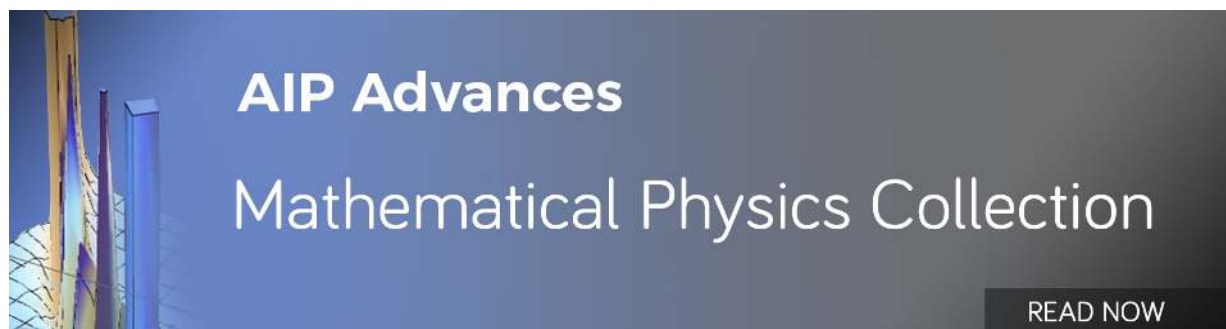Spherical magnetic nanoparticles fabricated by electric explosion of wire
AIP Advances **1**, 042122 (2011); https://doi.org/10.1063/1.3657510

Spherical magnetic nanoparticles fabricated by laser target evaporation
AIP Advances **3**, 052135 (2013); https://doi.org/10.1063/1.4808368

Co-precipitation synthesis of magnetic nanoparticles for efficient removal of heavy metal from synthetic wastewater
AIP Conference Proceedings **2124**, 020019 (2019); https://doi.org/10.1063/1.5117079

# Iron oxide nanoparticles fabricated by electric explosion of wire: focus on magnetic nanofluids

I. V. Beketov,[1,2] A. P. Safronov,[1,3] A. I. Medvedev,[1,2] J. Alonso,[4] G. V. Kurlyandskaya,[3,4,a] and S. M. Bhagat[5]

[1]*Institute of Electrophysics, RAS, Urals branch, Ekaterinburg, Russia*
[2]*Ural Federal University, Physical technology institute, Ekaterinburg, Russia*
[3]*Ural Federal University, Institute of natural sciences, Ekaterinburg, Russia*
[4]*Department of Electricity and Electronics, University of the Basque Country UPV-EHU Bilbao, Spain*
[5]*Department of Physics, University of Maryland, College Park, Maryland, USA*

Nanoparticles of iron oxides (MNPs) were prepared using the electric explosion of wire technique (EEW). The main focus was on the fabrication of de-aggregated spherical nanoparticles with a narrow size distribution. According to XRD the major crystalline phase was magnetite with an average diameter of MNPs, depending on the fraction. Further separation of air-dry EEW nanoparticles was performed in aqueous suspensions. In order to provide the stability of magnetite suspension in water, we found the optimum concentration of the electrostatic stabilizer (sodium citrate and optimum pH level) based on zeta-potential measurements. The stable suspensions still contained a substantial fraction of aggregates which were disintegrated by the excessive ultrasound treatment. The separation of the large particles out of the suspension was performed by centrifuging. The structural features, magnetic properties and microwave absorption of MNPs and their aqueous solutions confirm that we were able to obtain an ensemble in which the magnetic contributions come from the spherical MNPs. The particle size distribution in fractionated samples was narrow and they showed a similar behaviour to that expected of the superparamagnetic ensemble. Maximum obtained concentration was as high as 5 % of magnetic material (by weight). Designed assembly of de-aggregated nanoparticles is an example of on-purpose developed magnetic nanofluid. *Copyright 2012 Author(s). This article is distributed under a Creative Commons Attribution 3.0 Unported License.* [http://dx.doi.org/10.1063/1.4730405]

## I. INTRODUCTION

Magnetic nanoparticles (MNPs) of iron oxides exhibit unique and often advantageous properties suitable for a large variety of applications. Among other iron oxides, magnetite ($Fe_3O_4$) is one of the most versatile ferromagnetic materials with a high saturation magnetization, a Curie temperature well above the ambient, a relatively weak magneto-crystalline anisotropy and superparamagnetic behaviour in the fine particle state.[1,2] It is also widely available and relatively stable under ambient conditions.[3,4] Magnetite MNPs can be considered the most studied nanosized magnetic material designed for practical applications based firstly on its officially approved biocompatibility.[3,5] Nowadays, MNPs of the iron oxides have become important components in biosensing, magnetic separation, advanced medical screening and therapies, including bio-assays, magnetic resonance imaging (MRI), magnetically guided drug delivery, and hyperthermia, etc.[5–9] Thanks to a variety of excellent properties, magnetite MNPs were also used in many non-biological applications such

---

[a]Author to whom correspondence should be addressed. Electronic mail: galina@we.lc.ehu.es.

as storage media for magnetic memories, ferrofluids, magnetic separation, and catalysis.[6] In recent years, the $Fe_3O_4$ attracted additional attention due to the request from environmental applications in which it be used as an adsorbent due to the high adsorption capacity of magnetite MNPs for heavy metals and organic pollutants.[10]

Such a result would be not possible without enormous efforts in the development of fabrication,[11–14] characterization techniques[15, 16] and basic theory in the magnetism of the fine particles[17, 18] and assemblies of ferromagnetic nanoparticles.[19] There are different physical and chemical methods for fabrication of the oxide MNPs: hydrothermal synthesis,[11] microemulsion,[12] chemical co-precipitation,[16, 20] oxidation of $Fe(OH)_2$,[21] heating the material with different types of irradiation,[22] autocombustion,[4] and biomioneralization[23] etc. Despite the advantages of traditional chemical techniques for the iron oxide synthesis there are well known disadvantages, such as low production rates, limited purity or a high environmental cost of the final product, clear deviations from the sphericity, and wide size distributions, etc.

One of the relatively new techniques employed recently for iron oxides MNPs fabrication is an efficient and highly productive method based on the thermal dispersion of material in gas - the electric explosion of wire method (EEW). It is ecologically safe, provides production rates up to 200 g/h, requires a small energy consumption of about 25 kWh/kg and ensures a fabrication of MNPs with an average particle size of 20-100 nm, has a high degree of sphericity and a very small level of contamination.[24, 25]

The phenomenon of electric explosion of wire can be described as follows. A high-density ($10^4$-$10^6$ A/mm$^2$) current pulse (usually produced by the discharge of a capacitor bank) passes through the wire. In this case the density of the energy in the wire may considerably exceed the binding energy because of the high rate of the energy injection and the expansion lag of the heated material. As a result, the material boils to a burst and a mixture of superheated vapor and boiling droplets of the exploding material of wire scatter to the ambient atmosphere as a shockwave. Since explosion products expand as a cylinder with a much larger density than the density of the surrounding gas, oxidation takes place only on the surface of this cylinder while metal particles are formed inside the cylinder.[24, 26] This causes a decrease in the vapor concentration. Oxygen penetrates inside the cylinder of explosion products and brings about the process of burning and evaporating the formed metal particles and the subsequent condensation of the vapors to form the oxide particles. Since the vapor concentration lowers down and the melting point of oxides is much higher than the corresponding values for metals, the size of the oxide particles condensing during oxidation is much smaller than the size of the metal droplets.

The above mentioned effects were verified by a number of types of nanoparticles produced when the energy injected into the metal was much lower than the energy of evaporation: for $Al_2O_3$,[26] $TiO_2$, $ZrO_2$ and, in particular, for $Fe_2O_3$+$Fe_3O_4$[27] nanoparticles. It was found that in these cases the wires disintegrated into micrometer-sized particles which burned while they scattered in the oxidizing gas and left behind a vapor tail where the oxide nanoparticles were formed. Due to the decrease in the vapor concentration of the explosion chamber, it was possible to decrease the particle size to 15-20 nm, i.e., to increase the specific surface of powders to 80-100 m$^2$/g, without diminishing the production rate or rising the energy consumption. When the burning process is delayed, the specific surface of the oxide powders may be adjusted over broad limits due to the decrease in the oxygen concentration and, hence, the increase in the speed of the particles. In this case the powder presents a mixture of residual micrometer-sized particles and nanoparticles. Since the fraction of microparticles can be substantial and undesired for applications, a special fractionation system should be set up in the facility to separate nanoparticles.

The EEW production of powders is of special interest since a considerable overheat of the metal and the nonequilibrium process allows for the preparation of the nanoparticles with such new properties as well controlled sphericity and those which are expensive or difficult to produce by other methods. However, the application of EEW to the production of MNPs is not straightforward due to the strong tendency of interaction and aggregation of the MNPs. The air-dry assemblies of the MNPs prepared by many methods almost exclusively consist of aggregates formed by individual nanoparticles binded by strong magnetic interaction. It is also well known that fundamental magnetic characteristics such as coercive force and magnetic susceptibility are no longer constant material

characteristics in the nanoscale being dependent on the composition, size and shape of the MNPs.[1,3] Therefore, the necessary process of fractionation becomes very difficult and challenging.

In this work we describe our experience on preparation, fractionation and the step-by-step characterization of ensembles of magnetic nanoparticles of iron oxide produced by EEW using different chemical and physical techniques. The main focus was on the fabrication of the de-aggregated spherical magnetite nanoparticle ensemble with a narrow size distribution and the potential basis for the creation of on-purpose designed magnetic nanofluid.

## II. EXPERIMENTAL PROCEDURE, MATERIALS AND METHODS

### A. Method of electric explosion of wire

The method of electric explosion of wire was used for the fabrication of MNPs of iron oxide. The general view of EEW equipment designed at the Institute of Electrophysics of RAS (Ekaterinburg, Russia) is shown in Fig. 1. The roll of iron wire (carbon content 0.09%, diameter 0.47 mm) was positioned at the top of the feeding mechanism (1) which pushed the wire down into the reaction chamber (2) through a calibrated hole in the metal contact plate, playing the role of an upper electrode. The wire was constantly moved by the feeding device toward the metal contact plate (lower electrode) at the bottom of the chamber. Upper and lower electrodes were connected to the high voltage direct current source (3). The voltage applied to the electrodes was 30 KV and the distance between the contact plates was 220 mm. The high voltage source was concurrently recharged after each explosion. When the tip of the wire reached the lower contact plate, the voltage source discharged and the flowing electric current evaporated the leading end of the wire. After each explosion the feeding device kept advancing the wire, and the process was repeated again resulting in rapid production of MNPs.

The reaction chamber was filled with a circulating oxidizing mixture of 80% of $N_2$ and 20% $O_2$ flowing at 300 l/min, allowing oxidation of iron vapors and formation of iron oxide, rather than pure metal MNPs. The iron vapors formed oxide MNPs, which were driven by gas flow provided by the gas circulation fan (4) (Fig. 1). The obtained coarse MNPs were accumulated in the "cyclone" (5) while fine MNPs were accumulated in the "filter" (6).

During evaporation, a large amount of energy was released. In the segment of wire between the electrodes a thin plasma filament was formed and this area was heated up to $10^4$ K. Thereafter, hot iron vapors expanded in radial directions at an initial velocity of 2 km/sec, causing an explosion flash and a shock wave. Expanded iron vapors slowed down and cooled in the space of the reaction chamber condensing to the shape of MNPs. The electric energy applied to the wire was 40% of the sublimation energy of iron. This was found empirically to generate the nanoparticles of the smallest size. One can use an energy input lower than that needed for sublimation because of additional heating caused by the exothermic oxidation of Fe. The final elemental composition of the EEW prepared samples depended only on the chemical purity of the wire and the gaseous atmosphere ensuring a very small level of contamination.

### B. Structural characterization methods

The X-ray diffraction (XRD) study of MNPs was performed using the DISCOVER D8 (Bruker) diffractometer operating at 40kV and 40 mA with Cu-K$_\alpha$ radiation ($\lambda$ = 1.5418 Å) equipped with a graphite monochromator and a scintillation detector. The samples were mounted on a zero background silicon wafer fixed in a generic sample holder. A fixed divergence and antiscattering slit were used. Bruker software TOPAS-3 with Rietveld full-profile refinement was employed for the quantitative analysis of all the diffractograms. The initial Rietveld analysis allowed us to calculate the unit cell parameters, peak shape (Double-Voigt approach), background, systematic $2\theta$ shift, displacement, and half-width parameters for the profile function. Additionally the average size of coherent diffraction domains was estimated by using the Scherrer approach.[28,29] For transmission electron microscopy (TEM) the particles were sediment on carbon-coated copper grids. TEM was performed using a JEOL JEM2100 microscope operating at 200 kV.

FIG. 1. General view of equipment designed at the Institute of Electrophysics of RAS for production of metal oxide nanoparticls by the EEW method: 1 – wire feeding device, 2 – reaction chamber, 3 – high voltage source, 4 – gas circulation fan, 5 – cyclone, 6 – filter.

TABLE I. Selected physical properties of the EEW iron oxide MNPs: $d_n$, - number averaged mean diameter (TEM); $d_w$ - volume averaged mean diameter (TEM), $\delta$ − nonstoichiometry in $Fe_{3-\delta}O_4$ formula; $d_{XRD}$ - mean diameter defined by XRD.

| Sample | $d_n$, nm | $d_w$, nm | $S_{BET}$, m²/g | $\delta$ | Crystalline phase, % | $d_{XRD}$, nm |
|--------|-----------|-----------|-----------------|----------|----------------------|---------------|
| MC | 22 | 83 | 20 | 0.20 | Hematite 11.1 | 50 |
|    |    |    |    |      | Magnetite 88.9 | 90 |
| MF | 12 | 58 | 86 | 0.26 | Hematite 6.4 | 55 |
|    |    |    |    |      | Magnetite 93.6 | 35 |
| MC-1 | 6 | 10 | – | – | Hematite about 10 | 35 |
|      |   |    |   |   | Magnetite about 90 | ∼10 |
| MF-1 | 6 | 10 | – | – | Hematite below 5 | – |
|      |   |    |   |   | Magnetite above 95 | ∼6 |

The stoichiometric ratio $Fe^{2+}/Fe^{3+}$ in the MNPs was determined by Red-Ox potentiometric titration by potassium dichromate using an automatic titrator TitroLine (Schott Instruments). Titration was performed under an argon atmosphere in order to prevent oxidation of the $Fe^{2+}$ by the air oxygen. The non-stoichiometry of EEW iron oxide with regard to magnetite ($Fe_{3-\delta}O_4$) was calculated on the basis of the content of $Fe^{2+}$ and the total Fe content (Table I). The surface area of MNPs was measured by low-temperature sorption of nitrogen (BET) using Micromeritics TriStar3000 analyzer (Table I).

De-aggregation of MNPs in water suspension was studied by dynamic light scattering (DLS) using the Brookhaven ZetaPlus particle size analyzer. The electrokinetic zeta-potential of the suspensions was measured by electrophoretic light scattering (ELS) using the same analyzer. All the measurements were made at 298 K in suspensions diluted down to 0.1 g/L by de-ionized water. Ultrasound treatment of the suspensions for the de-aggregation was performed using a Cole-Palmer CPX-750 processor at a 300 W average power output level. Centrifuging of the suspensions was performed using a Hermle Z383 centrifuge with a 218 rotor at a maximum of 15 000 rpm.

## C. Magnetic and microwave characterization methods

Magnetic measurements of MNPs were performed at room and cryogenic temperatures using a vibrating sample magnetometer (Cryogenics Ltd. VSM), Physical Property Measurement System Quantum Design and a superconducting quantum device, SQUID (by Quantum Design MPMS-7). The magnetization values in a field of $5.2 \times 10^6$A/m were designated as the saturation magnetization, $M_s$. Primary magnetization curves were also measured for all cases in order to compare the demagnetizing fields of fabricated MNPs to demagnetizing fields estimated for ideally spherical MNPs with the same saturation magnetization.[30,31] Apart from the primary magnetization curves and the evolution of the magnetization as a function of the applied field at a constant temperature, the hysteresis cycles, M(H), typical zero-field cooled (ZFC) and field cooled (FC) thermomagnetic curves were measured for selected values of the applied magnetic field H = 3.95 kA/m and 7.9 kA/m.

Detailed descriptions of the microwave techniques, (i.e., ferromagnetic resonance (FMR) and non-resonant zero field absorption based on employing a conventional homodyne spectrometer and a half-wavelength rectangular cavity) were published in previous works of the Ferromagnetic Resonance Group at The University of Maryland.[4,25,31] The modulation technique was not employed since the FMR lines of the MNPs are broad: rather, we measured the microwave absorption (P) itself as a function of the applied field. The sample preparation procedure for microwave studies consisted of mixing MNPs with 7031 GE varnish and evenly spreading the mixture onto a 0.2 mm thick quartz plate. In order to study the possible effect of intergranular interactions, the MNPs were diluted by mixing them with non-magnetic talc powder in the volume ratios of 1 part in 6, followed by the spread onto the quartz plate with GE varnish. All microwave studies were done at room temperature and 8.85 GHz frequency (f).

## III. RESULTS AND DISCUSSION

### A. Structural characterization

Electron microscopy studies show that in all cases the EEW MNPs shapes are very close to spherical and their diameters lay within the 5 – 100 nm range (Fig. 2). The cyclon MC sample contains coarser MNPs with the presence of larger particles than the sample MF taken from the filter. Particle size distributions based on the graphical image analysis of TEM are given in Fig. 3. In addition, MC-1 and MF-1 samples after the MNPs separation (Table I) were also studied by TEM - these samples became almost identical after centrifuging (Fig. 3).

The highest probability given by the major maximum in both distributions corresponds to 10 nm particles. The fraction of particles with a size under 30 nm is 81% for MC and 96% for MF. Although the larger particles are present as the minor fraction, they strongly affect the magnetic behavior of EEW MNPs discussed below because the latter depends not only on the number of magnetic particles, but also on their cumulative volume. As particle size distribution (Fig. 3) is polydisperse, the number and volume averaged mean diameters ($d_n$ and $d_w$ respectively) can be calculated as follows:

$$\overline{d_n} = \frac{\sum d_i N_i}{\sum N_i} \tag{1}$$

$$\overline{d_w} = \frac{\sum d_i^4 N_i}{\sum d_i^3 N_i}, \tag{2}$$

where $N_i$ is the number of particles in the i-th fraction and $d_i$ is the particle diameter in the i-th fraction. The obtained values of $d_n$ and $d_w$ differ from each other in all cases under consideration (Table I).

Fig. 4 is an example of XRD spectra of MC and MC-1 MNPs. In all cases (see also Table I) XRD spectra were reasonably well fitted with the Rietveld method, and crystallographic parameters were defined for both observed crystallographic phases: magnetite (the phase responsible for the ferromagnetism of the system) and hematite. The typical cell parameter (a) for magnetite is a = 0.8396 nm. Slightly lower values (a = 0.8390 and a = 0.8368 nm for MC and MF, respectively) of the cell parameters were observed indicating that the type of structure can be defined as "defective spinel".[4] Generally, the unit cell of magnetite has 32 oxygen atoms and 24 Fe atoms, the latter are $Fe^{2+}$ and $Fe^{3+}$ on octahedral and tetrahedral sites. Their distribution among the octahedral sites is random and fluctuating.[2] It is a ferrimagnet so there is also competition between the sub lattices, and it is far from easy to tell how the absence of a set of neighbors would affect the alignment and modify magnetic properties.

The specific surface of MC MNPs evaluated from the TEM distribution (Fig. 3) is 19 $m^2$/g, which is in good agreement with the value obtained experimentally in BET sorption studies ($20\pm1$ $m^2$/g). The calculated specific surface area for MF MNPs is 62 $m^2$/g, which is less than that measured by adsorption ($86\pm1$ $m^2$/g) one. The difference most likely stems from underestimation of the number of the finest particles in TEM image analysis, which substantially contributes to high values of the specific surface area. The volume averaged mean diameters $d_w$ for both samples are in good agreement with the XRD results, which give $90 \pm 10$ nm and $35 \pm 8$ nm for magnetite crystallites in MC and MF cases, respectively. Thus, all structural data on EEW MNPs are self-consistent.

Although particles with a size under 30 nm dominate in EEW MNPs distribution (Fig. 3), a substantial amount of particles with diameters above the superparamagnetic limit[1,3] are still present both in MC and MF samples. Most likely this minor fraction of large particles is responsible for the ferromagnetic contribution in the case of as-prepared MNPs as shown in our previous report.[25] Therefore, the separation of large particles is a crucial requirement for the creation of on-purpose designed magnetic nanofluid containing de-aggregated spherical magnetite nanoparticles with a narrow size distribution. Conventionally, it is performed in liquid suspension of powder by the sedimentation procedure, which is based on Stokes's law,[4] for the velocity of sedimentation of
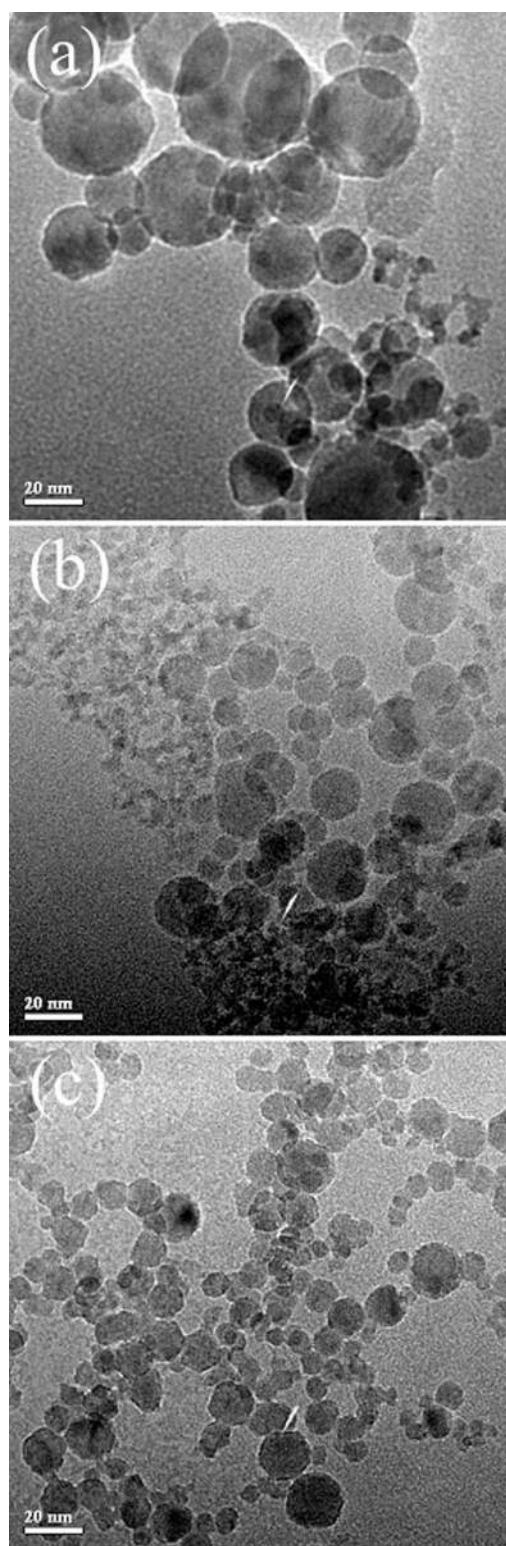
FIG. 2.  TEM images of EEW iron oxide MNPs: (a) sample MC taken from the cyclone, (b) sample MF taken from the filter, (c) sample MF-1 after separation (see also Table I).
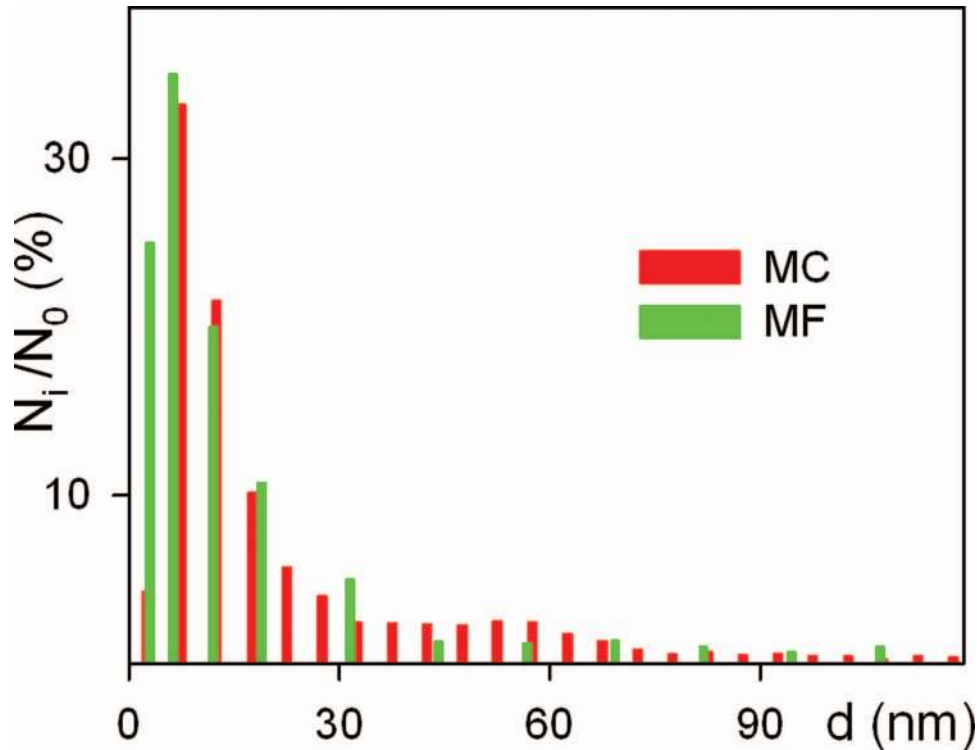
FIG. 3. Particle size distributions for EEW iron oxide MNPs.

spherical particles:

$$v = \frac{9}{2}\frac{R^2 g(\rho_2 - \rho_1)}{\eta}, \tag{3}$$

where R is the radius of the particle, g is the gravity acceleration, $\rho_2$, $\rho_1$ are the densities of the particle and carrier liquid respectively, and $\eta$ is the viscosity of the liquid. The velocity is proportional to the square of the particle radius, the large particles sediment faster than the small particles. Therefore it can be used for MNPs fractioning.

However, the fractioning of MNPs by sedimentation is not straightforward. First, due to their size, nanoparticles are involved in thermal motion, which is neglected in Stokes's law (Eq. (3)). This limitation can be overcome by making sedimentation in a centrifuge. Second, successful fractioning can be performed only when the powder is dispersed in liquid down to individual particles moving separately from each other. If particles of different sizes form aggregates in suspension it is impossible to separate them. The necessary condition of de-aggregation of particles in suspension is difficult to maintain in the case of MNPs.

Due to the high surface activity of nanoparticles they strongly tend to form aggregates in suspensions. Their inevitable aggregation during redispersion in liquid suspension is one of the main problems in processing air-dry nanopowders.[32,33] It is shown that methods such as ultrasonic dispersion[34] or high shear mixing[35] usually do not provide complete de-aggregation for non-magnetic oxides ($SiO_2$, $TiO_2$, ZnO, $Al_2O_3$). Meanwhile, dispersion and de-aggregation of magnetite air-dry powders is even more challenging as magnetic dipole-dipole interactions are also present apart from the interaction between MNPs driven by surface forces.

Thus, as the first step for the successful separation of large particles with residual ferromagnetism (MC and MF samples), we must achieve the de-aggregation of air-dry MNPs in suspension. Therefore, we performed special studies on the factors of the colloidal stability of EEW MNPs in water suspensions.

FIG. 4. XRD patterns for MC (a) and MC-1 (b) EEW MNPs. Points – experimental data; Bregg positions are shown by the colored bars: red bars are for hematite and blue bars are for magnetite. For interpretation of the references to color in this figure legend, the reader is referred to the web version.

EEW iron oxide MNPs do not form stable suspensions in pure water even if dispersed by ultra sound treatment. It means that as-prepared air-dry MNPs are strongly aggregated with each other due to a number of forces - these aggregates cannot be disassembled by thermal motion of water molecules. Apparently, some additional repulsive forces between nanoparticles in aggregates should be introduced to overcome their magnetic interaction and to provide further dispersion. Since the dominant magnetic interactions are long-range type interactions, the desirable repulsive force should be a long-range interaction as well. Hence, this might be a reason to establish electrostatic repulsion between magnetic nanoparticles for their de-aggregation.

For this purpose sodium citrate was selected as the electrostatic dispersant and stabilizer for metal oxide aqueous suspensions as it is widely used.[36] Upon the dissociation of sodium citrate in water the adsorption of citric acid anions onto the surface of metal oxide leads to the formation of a negatively charged layer, which provides electrostatic repulsion between particles and favors their de-aggregation. The mechanism of such electrostatic stabilization of the colloids based on the formation of a double electric layer is well known.[37] The electrostatic stability of colloid is characterized by the value of the electrokinetic ($\zeta$) potential, i.e., the electric potential on the plane between dense and diffuse parts of the double layer. It is known that the value of the $\zeta-$potential of about 40 mV, either positive or negative, provides electrostatic stabilization of colloid from coagulation.[38]

Fig. 5 shows the $\zeta-$potential of MC water suspensions stabilized by sodium citrate and the effective hydrodynamic diameter of nanoparticle aggregates depending on the pH of the suspension. Electrokinetic potential is highly negative at pH > 5, providing stabilization of suspension in neutral and basic conditions. The average hydrodynamic diameter of aggregates remains at a low and constant level in this pH range. In the acidic conditions at pH < 5, citrate anions begin to reassemble
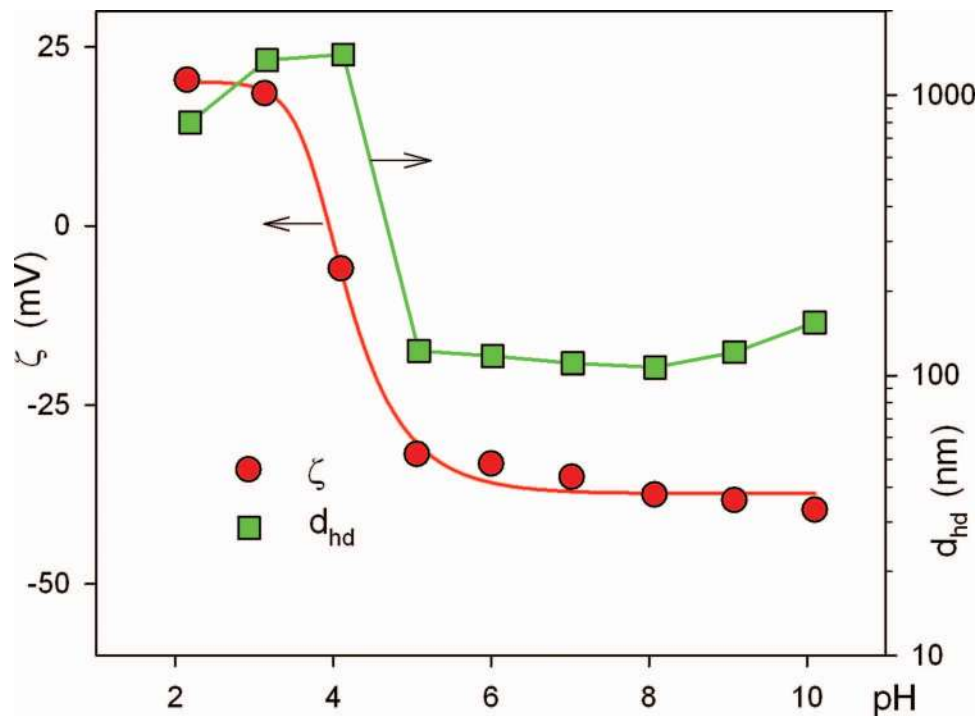
FIG. 5. PH dependence of electrokinetic potential (1) and the effective hydrodynamic diameter of aggregates (2) in an aqueous suspension of MC EEW iron oxide MNPs stabilized with sodium citrate. Lines are drawn as eye-guide only.

with protons in a water solution forming uncharged molecules of citric acid, which cannot stabilize the suspension electrostatically. As a result, the absolute value of the $\zeta$-potential vanishes at pH = 4, the average hydrodynamic diameter of aggregates sharply increases and the suspension coagulates. At pH < 3 the $\zeta$-potential becomes positive, likely due to the adsorption of protons on the particle surfaces. However, the value of the $\zeta$-potential +20 mV is too low for the stabilization of suspension, and the diameter of aggregates in acidic solution is much higher than in the basic conditions.

Stabilization of EEW MNPs suspensions by sodium citrate is also influenced by the concentration of dispersant. Figure 6 shows the dependence of the $\zeta-$potential and the effective hydrodynamic diameter of MNPs aggregates on the concentration of sodium citrate in MC suspensions. The electrokinetic potential of MC suspensions remains almost constant (about –40 mV) if the concentration of sodium citrate is in the range of $3 \times 10^{-4}$ to $3 \times 10^{-2}$ M. It means that double electric layers on particle surfaces do not change very much while there is a variation of the stabilizer concentration. If the concentration of sodium citrate is increased above this upper level, the absolute value of the $\zeta$-potential gradually diminishes due to the contraction of the double layer at a high ionic strength of the solution.[37] Thus, a sodium citrate concentration $3 \times 10^{-2}$ M might be considered the upper limit for effective stabilization of EEW iron oxide MNPs suspensions. In further studies we used $5 \times 10^{-3}$ M sodium citrate in order to stabilize the suspensions, which correspond approximately to the middle part of the concentration range.

Although the $\zeta$-potential decreases with an increase in concentration of sodium citrate above $3 \times 10^{-2}$ M, the average hydrodynamic diameter of aggregates in EEW iron oxide MNPs suspensions does not increase until sodium citrate concentration exceeds $2 \times 10^{-1}$ M. At this concentration, the $\zeta$-potential is close to –30 mV, which is still sufficient for suspension stabilization. However, the double layers on particle surfaces are thinned to a certain extent. At higher concentrations of sodium citrate (up to 3 M) the diameter of aggregates substantially increases and the suspension coagulates.

Thus, based on the study of the electrostatic stabilization of EEW iron oxide MNPs suspensions, we have chosen the optimum concentration of sodium citrate 5mM at a neutral pH as the necessary condition for the de-aggregation of MC and MF dry MNPs in water. However, it is clear (Figs. 5 and 6)
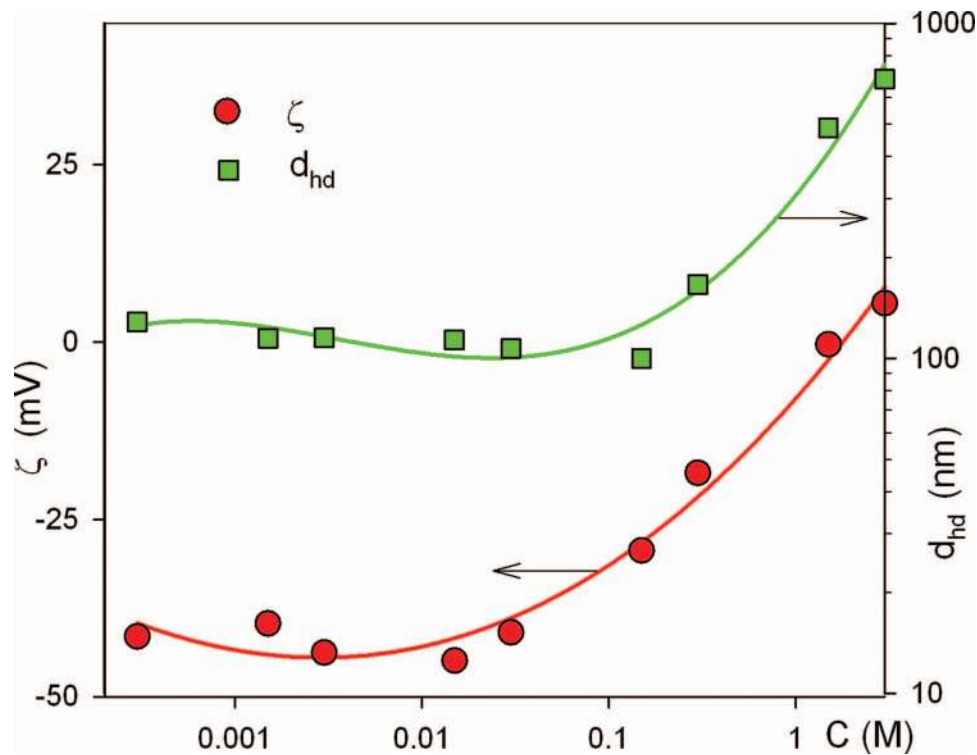
FIG. 6. Dependences of electrokinetic potential (1) and effective hydrodynamic diameter of aggregates (2) in aqueous suspension of MC EEW iron oxide MNPs on a concentration of sodium citrate. Lines are drawn as eye-guide only.

that the average hydrodynamic diameter measured by DLS in MC and MF suspensions is still much higher than that measured by TEM in powders. It means that complete de-aggregation is not spontaneous even if the appropriate dispersant is used.

Fig. 7 shows weight average size distributions for MC and MF suspensions in 5 mM sodium citrate measured by DLS. Both suspensions were dispersed by ultra-sound treatments for 20 min. Distributions for both samples are bimodal, indicating that such a regime of dispersion does not provide entire de-aggregation of particles in suspension and large amounts of aggregates are still present even in electrostatically stabilized suspensions of magnetite. The size of aggregates falls within 200 – 400 nm range which makes them involved in thermal motion. This therefore prevents their separation by sedimentation.

Further de-aggregation of MC and MF suspensions was performed by excessive ultrasound treatment. Fig. 8 shows the diminishing of average hydrodynamic diameters of MNPs aggregates in MC and MF suspensions during ultrasound treatments over the course of time. The plots are well fitted by the following exponential decay functions: $d_{hd} = 112 + 310 \times e^{-0.026t}$ (MC) and $d_{hd} = 119 + 1450 \times \exp^{-0.029t}$ (MF). Both samples reach almost the same de-aggregation level of about 115 $\pm$ 4 nm after 180 min of ultrasound treatment.

Fig. 9 presents Log-normal intensity weighted particle size distribution in suspensions after excessive ultrasound treatment obtained by DLS (marked by diamonds). The histogram (filled red) in Fig. 9 corresponds to the weighted particle size distribution recalculated from the number particle size distribution of the MF sample presented in Fig. 3. Both distributions are in good agreement. Thus, it may be concluded that a 180 min ultrasound treatment of the suspensions leads to a complete de-aggregation of MC and MF suspensions.

Data for the MF sample in Fig. 9 supports the above conclusion that particle size distribution of as-prepared EEW iron oxide MNPs is too wide and contains particles with diameters well above 100 nm. The contribution of these particles to the intensity of light scattering is large because it
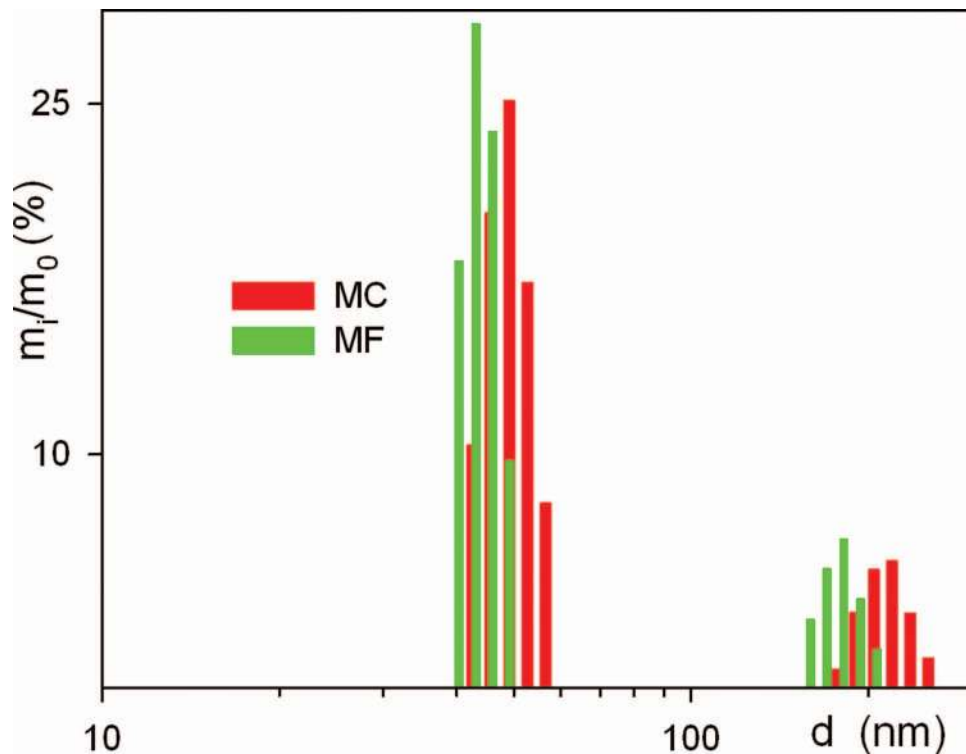
FIG. 7. Bimodal distribution of MC and MF EEW iron oxide MNPs in suspension in 5 mM sodium citrate.

is proportional to the 6th order of the particle diameter.[39] Meanwhile, the relative number of such particles is low according to the number distribution of the MC sample (Fig. 3).

After successful de-aggregation of air-dry MC and MF powders in aqueous suspensions we were then able to perform fractioning on them by sedimentation in order to remove the minor fraction of large particles. This was done by centrifuging de-aggregated suspensions of MC and MF for 5 min at 18000g. The fractioning was performed with both MC and MF samples obtaining MC-1 and MF-1 samples. Figure 2(c) shows the TEM image of fractionated MF-1 EEW iron oxide MNPs. Weighted particle size distribution for the MF-1 sample was obtained using TEM image analysis. It is shown by the histogram filled in blue in Fig. 9 for comparison with the distribution measured by DLS in the MF-1 suspension (marked by circles). It can be seen that both distributions correlate fairly well. Maximum obtained concentration was as high as 5 % of magnetic material (by weight). This result might be evidence for the successful separation of superparamagnetic fraction from air-dry EEW iron oxide MNPs.

The resulting MC-1 and MF-1 suspensions have virtually the same DLS hydrodynamic particle diameter of $50 \pm 2$ nm and the same intensity weighted particle size distribution (figure 9). The suspensions of MC-1 and MF-1 were then mixed with the excess of acetone to provide precipitation of EEW iron oxide MNPs. Thus, dry samples of MC-1 and MF-1 were obtained.

## B. Magnetic and microwave characterization

### 1. Magnetic characterization

Fig. 10 shows the magnetization as a function of the temperature obtained in zero-field-cooling and field-cooling processes with an applied field of 3.95 kA7m. For the ZFC data, the samples were cooled at zero-field from room temperature down to 5 K, and then the magnetization was recorded with an increasing temperature while applying a constant magnetic field. For the FC data, the process was repeated, but with the same magnetic field also applied while cooling. In the MF and MC MNPs
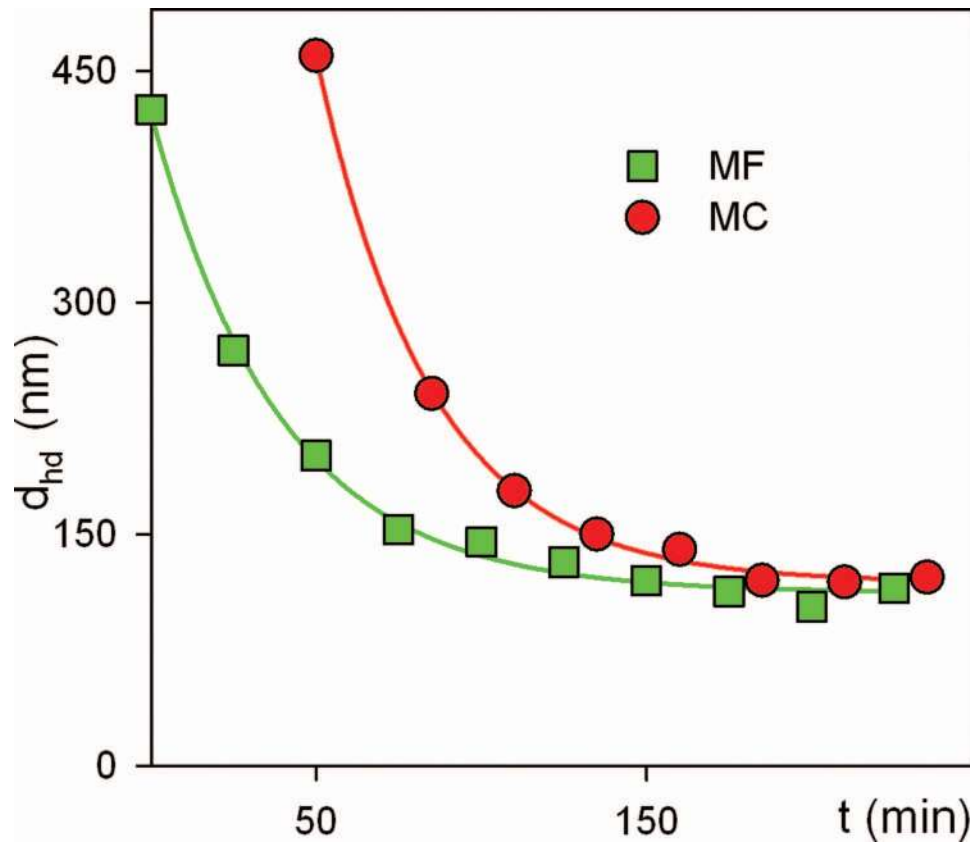
FIG. 8. Dependence of the average hydrodynamic diameter in suspensions of MC and MF EEW iron oxide MNPs on the duration of ultrasound treatment.

the FC magnetization keeps fairly constant within the range of temperatures studied and there is no clear maximum in the ZFC (Fig. 10). One can observe a small difference in FC behaviour of MF and MC samples: in the last case the magnetization jump is seen near 90 K, which is probably associated with a Verwey transition (VT) in big MNPs of magnetite.[40] This supposition is consistent with the XRD analysis: in as-prepared MF and MC samples the average sizes were around 35 and 90 nm, respectively. The absence of a VT is typical of small magnetite nanoparticles with diameters below 50 nm.[41,42]

Although the magnitudes measured for MF-1 and MC-1 samples are quite similar, the shapes of their ZFC-FC curves are very different compared to the MC and MF samples (Fig. 10). Apart from the complete disappearance of the Verwey transition, a broad maximum appears in the ZFC curves of both MC-1 and MF-1 samples. This clearly reveals that the fractioning method by centrifuging has been fruitful, and the MC-1 and MF-1 samples present a magnetic behaviour much more similar to the one expected for a superparamagnetic (SPM) ensemble of small MNPs. In the case of SPM non-interacting nanoparticles, this maximum is related to the blocking temperatures of their magnetic moments: at high temperatures, above these blocking temperatures, the magnetic moments are fluctuating along the easy axis of each nanoparticle, and the observed average magnetic moment, within the time-scale of the experiment, is null. However, as the temperature decreases, thermal fluctuations diminish, and the magnetic moments become progressively *blocked*, at first the biggest nanoparticles and the smallest ones last.

A broad maximum of the FC curve, such as one observed in MF-1 and MC-1 cases, could, in principle, be related to a wide distribution of MNPs sizes, or to the effect of the interparticle interactions. The importance of the interparticle interactions is confirmed by the fact that the magnetization does not decrease down to zero even at room temperature, as would happen in a pure
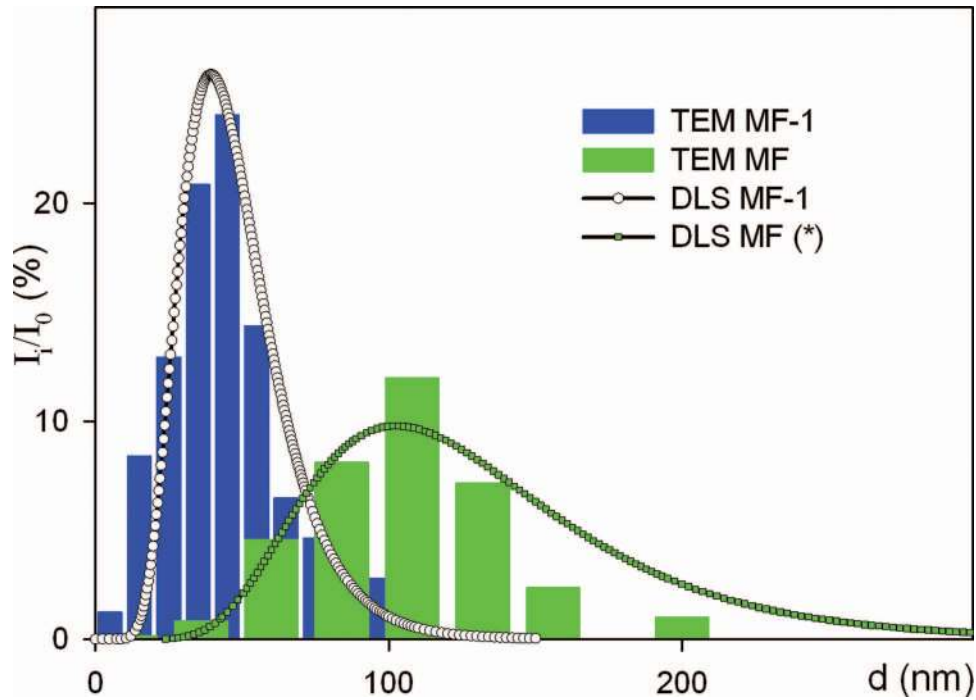
FIG. 9. Comparison of intensity weighted particle size distributions for MF EEW iron oxide MNPs measured by DLS and TEM. Notation MF corresponds to the initial EEW nanopowder. Asterisk * relates to the suspension subjected to the extensive ultrasound treatment for 180 min. MF-1 corresponds to the fraction separated by centrifuging.

TABLE II. Selected properties of the EEW MNPs. Magnetite MNPs magnetization value measured at a temperature of 300 K for the field of 65 kOe was designated as $M_s$; $H_c$ – coercivity measured at room temperature. $\mathbf{M_s}^*$ - magnetization value recalculated for the internal volume of the MNPs corresponding size, i.e., without the volume corresponding to about two surface layers.

| Sample | $M_s$ (kA/m) | $V_{surf}/V(\%)$ | $M_s^*$ (kA/m) |
|---|---|---|---|
| MC | 415 | 10 | ~470 |
| MF | 290 | 25 | ~390 |
| MC-1 | 100 | 70 | ~330 |
| MF-1 | 90 | 90 | ~450 |

non-interacting SPM system. Concerning the nature of these interactions, it would be reasonable to assume, taking into account that our samples are ensembles of magnetite nanoparticles, that mainly short-range ferromagnetic interactions are present. At the same time, according to XRD analysis, one must also consider the presence of hematite (up to 10 at. %), which can, to a certain extent, act as a separator between the magnetite MNPs. Therefore the long-range dipolar interactions could also be relevant. Additionally, taking into account the small size of the MNPs in MC-1 and MC-1 samples, the relative amount of atoms on their surface is going to be very important (above 70 % for small MNPs with a $\approx 0.84$ nm). Fig. 11 shows the characteristic ratio of the surface volume ($V_{surf}$) corresponding to the first two atomic layers to total volume (V) of the nanoparticle as a function of the diameter of the magnetite MNPs. Since the surface atoms have fewer nearest neighbours than those inside the nanoparticles, they can also affect the transmission of the short-range interactions between the nanoparticles (see also Table II).

The ZFC-FC curves of MC-1 and MF-1 samples are very similar in magnitude and shape, although there is a small displacement of the maximum of the ZFC curve for the MC-1 sample towards higher temperatures. This suggests a slightly bigger average size for the magnetite nanoparticles in this sample in plausible agreement with the XRD results. In order to obtain information about the
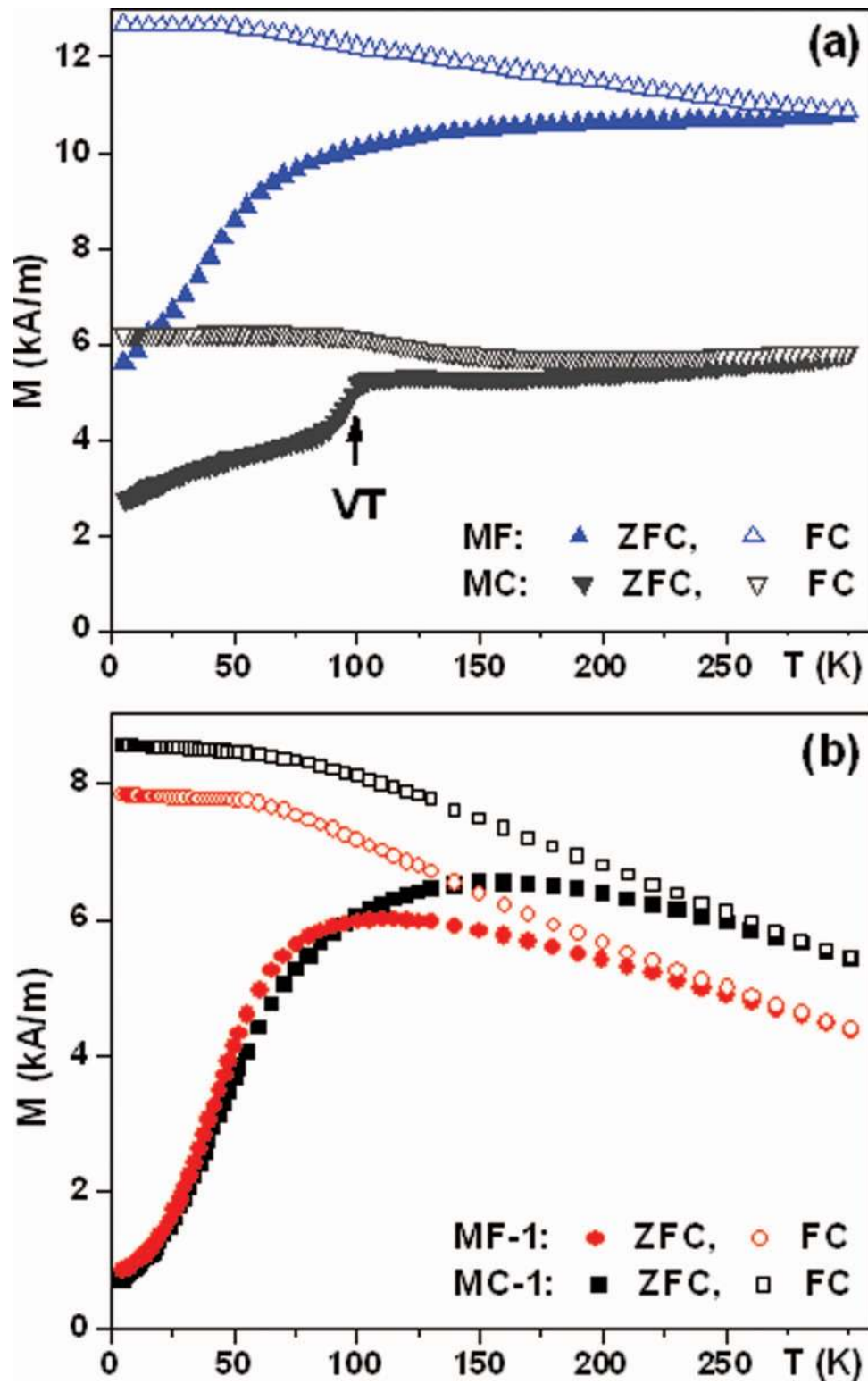
FIG. 10.  ZFC-FC curves measured with $H = 3.9$ kA/m for the MF, MC (a) and MF-1 MC-1 (b) samples. Dashed line (a) indicates a Verwey transition (VT) temperature.
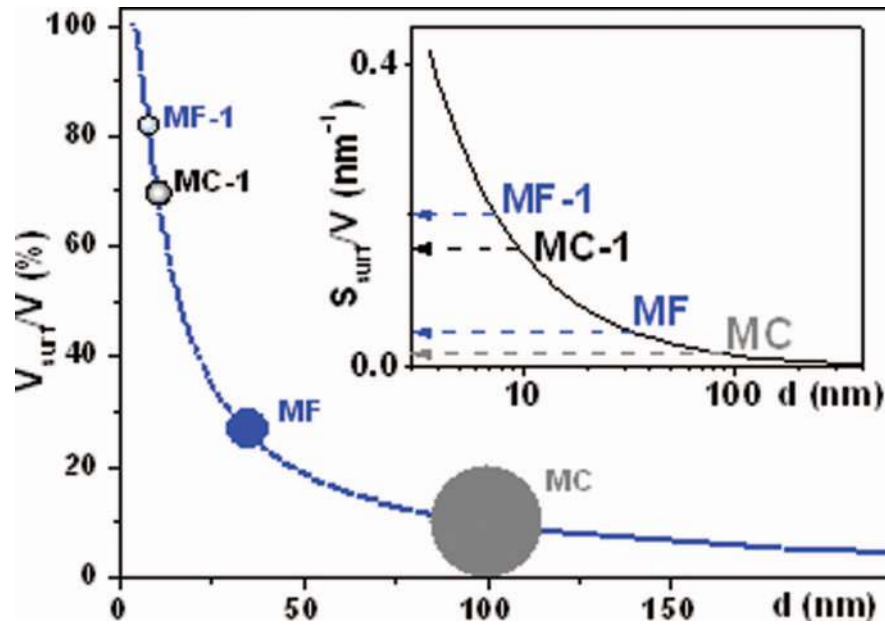
FIG. 11. Evolution of the relative amount of atoms on the surface of the magnetite nanoparticles (2 atomic layers) as a function of the MNP sizes. Inset, shows the evolution of the surface to volume ratio for magnetite nanoparticles. The diameters of the MF, MC, MF-1 and MC-1 samples are shown in the correct scale.

TABLE III. Average diameters, $D$, standard deviations, $\sigma$, and anisotropy constants, $K$, obtained from the fittings of the ZFC curves to Eq. (4), and from the fittings of the hysteresis loops to Eq. (5).

| Sample | ZFC-FC | | | $M$ (H) loops | |
|---|---|---|---|---|---|
| | $D$ (nm) | $\sigma$ (nm) | $K$ (J/m$^3$) | $D$ (nm) | $\sigma$ (nm) |
| MC-1 | 8.4 | 1.9 | $1.2 \times 10^5$ | 8.0 | 0.9 |
| MF-1 | 7.3 | 1.8 | $1.3 \times 10^5$ | 7.0 | 0.8 |

size and anisotropy of the magnetite nanoparticles, we have fitted the ZFC curves of the MC-1 and MF-1 samples to an expression which considers a coherent rotation of the magnetic moments inside each nanoparticle during the relaxation processes:[43,44]

$$M_{ZFC}(T) = M_0 \int_0^{V_C} L\left(\frac{\mu_0 M_S V H}{k_B T}\right) f(V)dV + \left(\frac{M_0 M_S H}{3K}\right) \int_{V_C}^{\infty} f(V)dV \tag{4}$$

being $L(x)$ a Langevin function: $L(x) = \coth(x) - 1/x$, and $M_0$ is the magnetic saturation of the sample, as a whole. This simplified model assumes that the nanoparticles present a size distribution, $f(V)$, being $V$ the volume of each nanoparticle; that each nanoparticle has an average a uniaxial anisotropy, $K$, and a saturation magnetization, $M_S$; and that no interactions between them are present. Even if this is not really the case for present ensembles, it is interesting to carry out the fitting for obtaining a preliminary estimation of the size and anisotropy of the MNPs. The fittings have been performed fixing $M_S$ to 480 kA/m, and the saturation magnetization value of the *bulk* magnetite and $M_0$ to 104 kA/m, the saturation magnetization value of the sample indicated by the hysteresis loops, measured in present studies (Fig. 12). As we have shown. a good fitting has been obtained, assuming a log-normal size distribution for the MNPs. The calculated average diameters, $D$, standard deviations, $\sigma$, and anisotropy constants, $K$, are presented in Table III. As indicated, the magnetite nanoparticles exhibit a relatively narrow size distribution, with average sizes close to those estimated by XRD (6 and 10 nm) and TEM (10 nm). The anisotropy values are very similar for both MF-1 and MC-1 samples, and they are an order of magnitude greater than that measured in bulk magnetite ($\sim 1.35 \ 10^4$ J/m$^3$), as it is usual in nanoparticles.
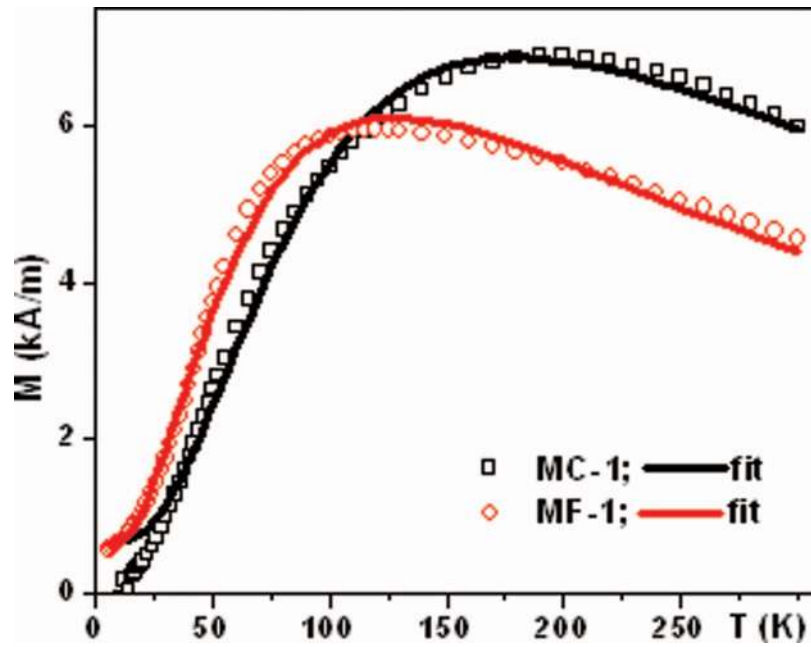
FIG. 12. ZFC curves measured with $H = 3.9$ kA/m for the MF-1 and MC-1 samples, and the corresponding fittings (black lines) to Eq. (4).

In order to obtain more information about the magnetic behaviour of the samples, we have also analyzed the magnetic response of the system as a function of the applied magnetic field. This was done by measuring the hysteresis loops, M vs. H, at low (5 K) and high (300 K) temperatures, with magnetic fields up to 65 kOe. Fig. 13 shows the M(H) loops of the samples after fractioning. The absence of hysteresis at room temperature, as depicted in the insets and the shape of the hysteresis loops is typical of SPM systems. In this type of system, at low temperatures when the MNPs are blocked, the magnetization process with an increasing magnetic field is associated with the rotation of the magnetic moment of each nanoparticle towards the direction of this magnetic field. This is an energetically expensive process that gives rise to high coercivity and non-zero remanence values. As the temperature increases, thermal fluctuations give rise to a SPM state, characterized by a null coercivity and a non-saturating behaviour, which follows a Langevin expression with a diameter distribution function, $f(D)$:

$$M(H) = M_0 \int_0^\infty L \left( \frac{\mu_0 M_S V H}{k_B T} \right) f(D) dD \qquad (5)$$

For both MF-1 and MC-1 samples, similar and high coercivity ($H_c \approx 50$ kA/m) and low remanence ($M_r/M_s \approx 0.22$) values were obtained at a low temperature. The fact that $M_r/M_s$ at 5 K is below 0.5 is rather telling because 0.5 is the expected value for a non-interacting 3-D system with random anisotropy. The obtained magnetic characteristics could be due to the effect of the interparticle interactions and their non-uniform distribution.[19,46]

It is also interesting to mention that even at 5K, the magnetization curves do not saturate and the maximum magnetization ($\sim$130 kA/m) value is appreciably smaller than the one expected for bulk magnetite ($\sim$480 kA/m). This can be understood by taking into account again the small size of the MNPs and the high amount of atoms on the surface, as discussed before (Fig. 11, Table II). Consequently, it is more difficult to align the surface spins in the direction of the magnetic field, giving rise to observed non-saturating hysteresis loops.

We have pursued a better insight of these measurements by fitting the hysteresis loops measured at room temperature to Eq. (5) in order to obtain a new estimation of the average size of the magnetite nanoparticles. The corresponding fittings are plotted in Fig. 14. As represented, a good fitting has been obtained using a log-normal size distribution. The corresponding $D$ and $\sigma$ values are indicated
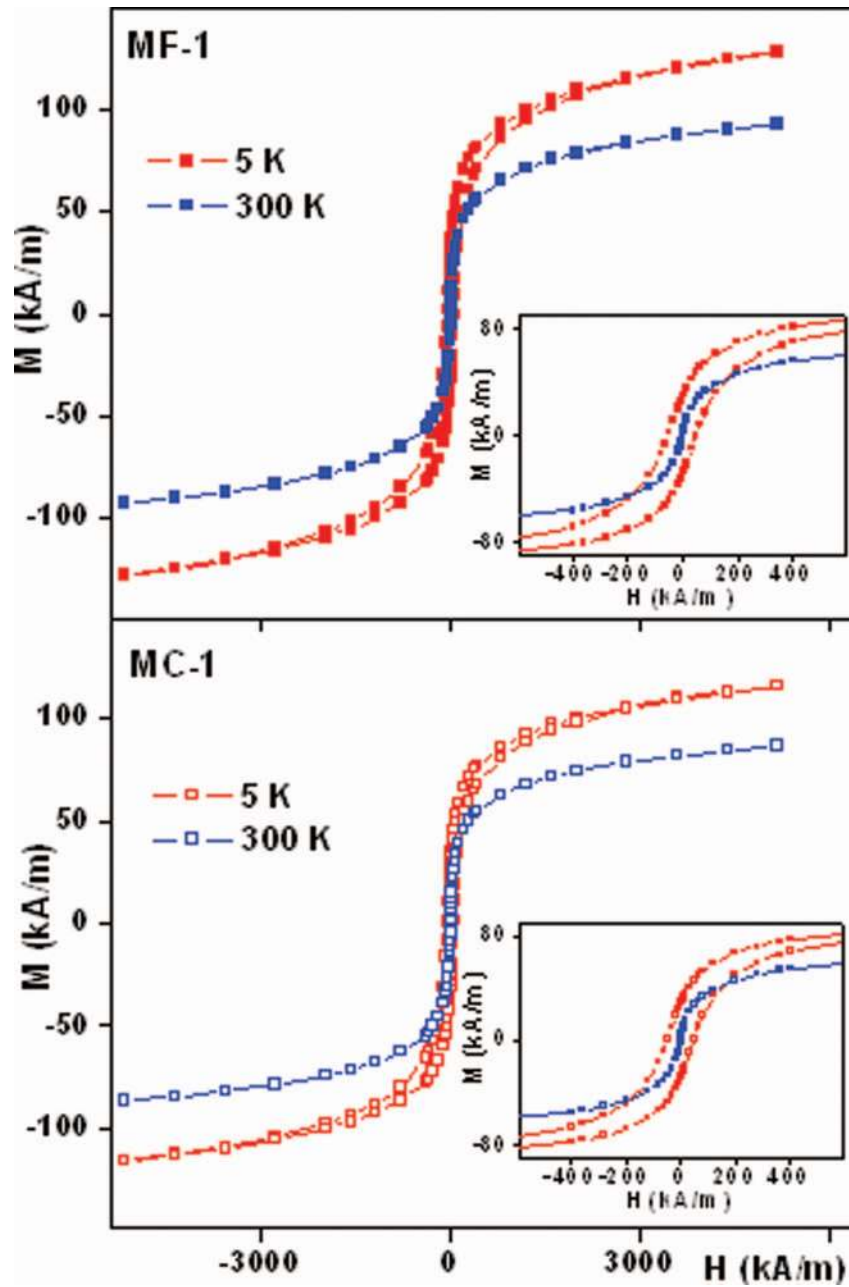
FIG. 13. Hysteresis loops measured at 5 and 300 K for the MF-1 and MC-1 samples. The insets present, a zoom-in of the hysteresis at low fields.

in Table III. As observed, the obtained values are in good agreement with those estimated by the previous fittings of the ZFC curves, and again this confirms that the behavior of MF-1 and MC-1 nanoparticles is close to SPM, despite the presence of interactions.

It is interesting to compare the hysteresis loops of the samples before (MC and MF) and after fractioning (MF-1 and MC-1). For example, Fig. 15(a) shows the hysteresis loops of MC and MC-1 MNPs at room temperature - there is a clear difference between theses two ensembles. It is evident from the shape of the M(H) loop that a SPM-like behaviour was not observed for MC and MF systems. This is probably due to the bigger size of the MNPs, and/or clustering processes, as suggested also by the higher value of the saturation magnetization. It was also confirmed by a bad
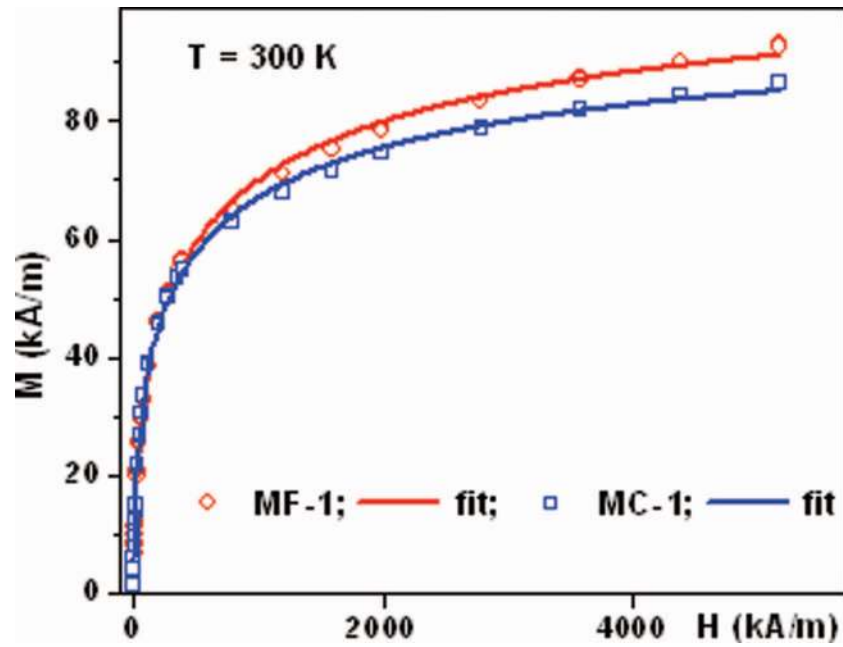
FIG. 14. Hysteresis loops measured at 300 K for the MF-1 and MC-1 samples, and the corresponding fittings (black lines) to Eq. (5). Inset shows low field behaviour of MF as prepared sample with relatively high coercivity and MF-1 practically unhysteretic behaviour of the same sample after separation by centrifuging.

fitting of the hysteresis loop of the MC sample to Eq. (5), as depicted in figure 15, which gave very small unrealistic values for the standard deviation of the nanoparticle sizes ($\sigma = 0.01$).

In light of Fig. 11 we have recalculated the saturation magnetization values for the reduced effective volume of the MNPs of the corresponding size, i.e., without the volume corresponding to two surface layers (Table II, $M_s{}^*$ data). One can see that the obtained numbers are closer to the value of the saturation magnetization of the bulk magnetite,[45] although there are still some deviations. We also have a simple analysis of the primary magnetization curves successfully employed earlier for different kinds of MNPs.[25,30,31] These results are shown in Fig. 15(b). For a single separated particle one can express the magnetic field, $H_{eff}$, sensed by the particle as follows:[47]

$$H_{eff} = H - DM \tag{6}$$

where H is the applied field, D is the demagnetizing factor, and M is the magnetization. Therefore:

$$M = \chi(H - DM) \tag{7}$$

where $\chi$ is the magnetic susceptibility. The measured quantity, an effective susceptibility, $\chi_{eff}$, can therefore be described as:

$$\chi_{eff} = \frac{M}{H} = \frac{\chi}{\frac{1}{\chi} - D} \tag{8}$$

If $\chi >> 1$, $\chi_{eff}$ is controlled only by the demagnetizing factor. For a magnetic sphere all components of the demagnetizing field are equal to each other: $Dx = Dy = Dz = \frac{1}{3}$. Hence for the linear part of the primary magnetization curve one can write M = 3H. Such a relation is useful for simple evaluation of the shape of the magnetic nanoparticles as shown prior.[30] In our previous publications we have shown the validity of the evaluation of the initial slope of the M vs. H curve which was close to 3 for spherical nanoparticles.[25,31] Any deviation from this position means deviation from the spherical shape reflected by the contribution of the demagnetizing fields. At the same time this analysis is only valid for ferromagnetic nanoparticles. When the size of MNPs goes down to the superparamagnetic limit the analysis of the primary magnetization curve for the shape evaluation becomes more complex (Fig. 15(b)). Even so, we observed M ≈ 3H using the initial slope of the
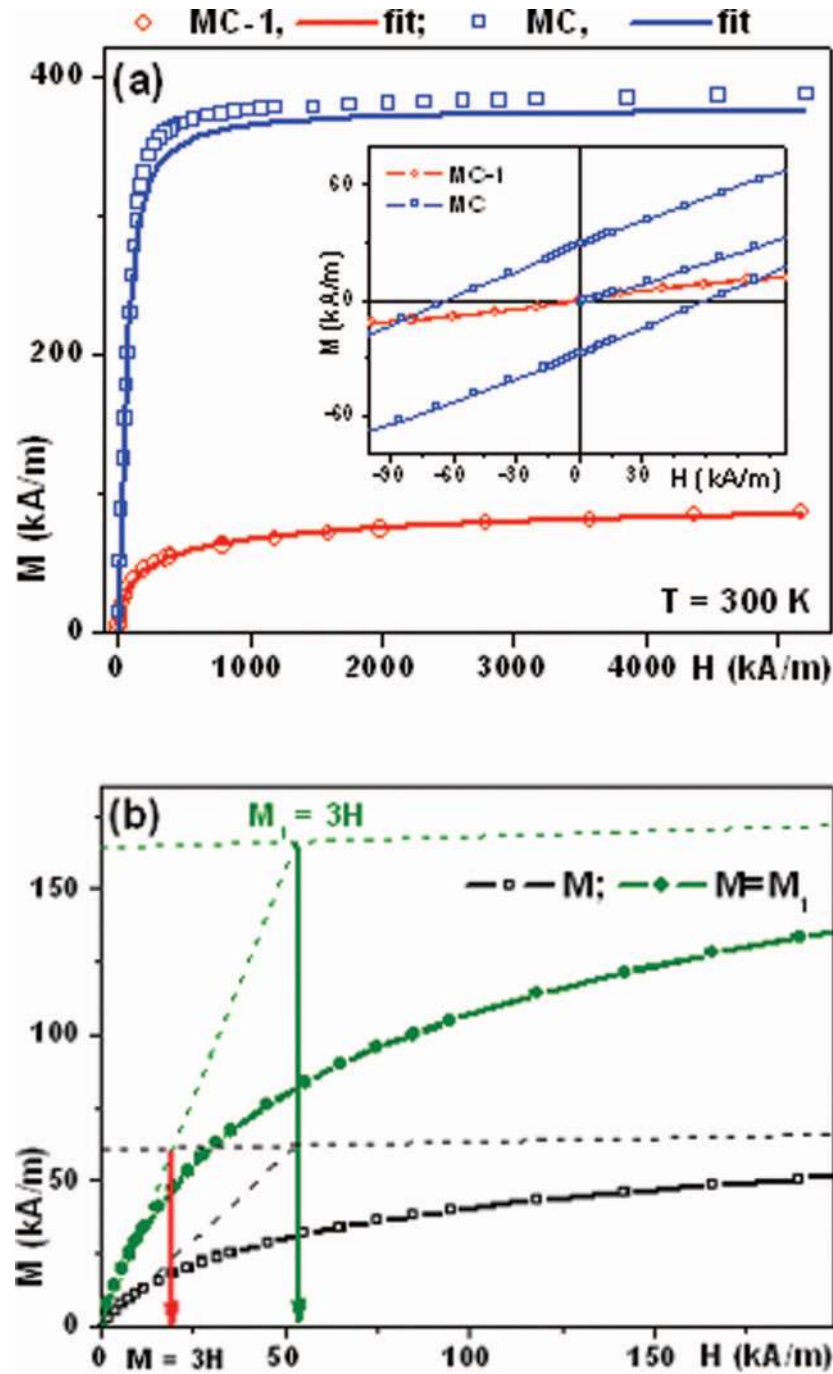
FIG. 15. Comparison of the hysteresis loops measured for MC-1 and MC samples at room temperature. Inset shows low field behaviour of the MC as-prepared sample with a relatively high coercivity and practically unhysteretic behaviour of the MF-1 sample after separation by centrifuging (a). Analysis of the shape of the MNPs using initial slope of the magnetization curve and the saturation approach slope (b): red arrow indicates the position for experimental data cut point of the initial slope and saturation approach lines of MF-1 MNPs; green arrow indicates the position for M = 3H of MF-1 MNPs value for $M_1$ recalculated in supposition of 10 nm diameter nanoparticle with a "magnetic core" of about 7 nm.

TABLE IV. Microwave absorption results for iron oxide MNPs: $H_{res}$ is a resonance field for $H_{dc} \perp h_{rf}$; $\Delta H$—line width at half the peak intensity. Frequency f $\approx$ 8.85 GHz.

| | $H_{res}$ (kA/m $\pm$ 10) | | $\Delta H$ (kA/m $\pm$ 15) | | |
|---|---|---|---|---|---|
| Sample | Without talc | With talc | Without talc | With talc | Zero field absorption |
| MF | 240 | 245 | 100 | 80 | Low |
| MC | 220 | 230 | 140 | 160 | High |
| MF-1 | 240 | 245 | 80 | 60 | No |
| MC-1 | 245 | 245 | 80 | 55 | No |

magnetization curve and the saturation approach slope cut point for MF-1 MNPs experimental data. If we consider a "magnetic core" of 7.3 nm in diameter for MF-1 MNPs (Table II), the precise position M = 3H can be obtained supposing that the surface layer of 3 nm does not contribute to the ferromagnetic response of the assembly. In this case the average diameter of about 10 nm must be considered. One should develop a more precise model in order to prove the above mentioned supposition about the 3 nm shell non-magnetic layer, first asking how many nearest and next-nearest neighbours are necessary for FM alignment in a defective spinel. This component lies far from the objectives of our present work. It is something to be developed in a future.

In summary, the magnetic measurements confirm that using the EEW as a fabrication method followed by the separation from centrifuging, we were able to obtain small magnetite nanoparticles with a relatively narrow size distribution, and that despite the presence of magnetic interactions between the MNPs, they present behaviour similar to that expected of an ensemble of SPM nanoparticles.

### 2. Microwave Characterization

Fig. 16 and Table IV show a summary of the microwave studies of the samples placed at the bottom of the cavity using the standard cavity perturbation technique.[4,25] The external dc field (H) was perpendicular to the microwave magnetic field $h_{rf}$. From the very beginning it is important to indicate that MC and MF MNPs ensembles are very different from MC-1 and MF-1 MNPs. In the first case we are dealing with systems which have significant coercivity (of the order of 60 kA/m at 300 K) and ferromagnetic contributions. In the second case (MC-1 and MF-1) MNPs can be described as systems with close to zero coercivity and superparamagnetic behaviors. Despite clear differences in the magnetic state of the MNPs systems their microwave behaviour has many common features.

For all types of studied MNPs only one FMR resonance line was observed, i.e., the obtained materials were magnetically uniform (Table IV). At the same time, in addition to the resonant response, both MF and MC samples showed significant zero-field absorptions, which is attributed to Joule heating consequently on the e-fields generated by the time-varying b-field in the conducting powders.[4,48] At the same time the oxides are essentially non-conducting. Our previous structural studies[25] have shown that this effect most likely occurs because of the inclusion of some metallic iron in the biggest particles due to their partial oxidation in the centre. As expected, one can see that separation by centrifuging results in the complete disappearance of the zero-field absorption for all the samples since ensembles with a narrower size distribution a and smaller average size contain no big particles with a metallic centre.

For spherical MNPs, if the contributions from stresses and magnetocrystalline anisotropy were negligible - for f = 8.85 GHz, one would expect $H_{res}$ to be about 240 kA/m using g = 2.12, which is appropriate for the $Fe_3O_4$ system.[16,49] For such spherical MNPs the resonance field can be given by a familiar formula:
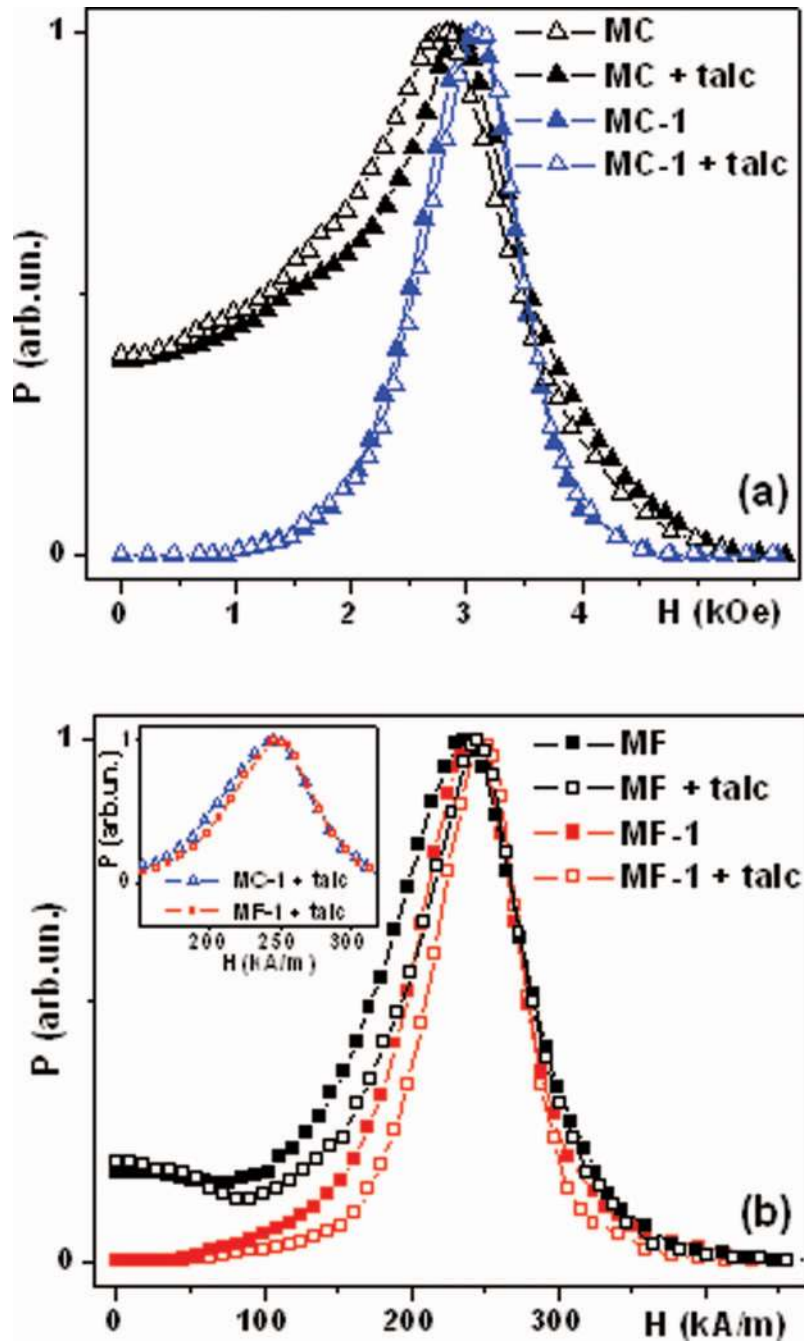
$$\frac{\omega}{\gamma} = H_{res} \tag{9}$$

FIG. 16. Microwave losses (P) at f = 8.85 GHz as a function of the external magnetic field (H) for MNPs produced by EEW: MC and MC-I (a); MF and MF-I (b). MC and MF – as prepared samples; MF and MF-1 – the same samples after separation by centrifuging. Inset shows for comparison EEP MNPs from the cyclone and filter with the narrowest line width.

where $\omega = 2\pi f$ is the microwave frequency and $\gamma$ is the gyromagnetic ratio: $\gamma = 1.1 \times 10^5 g \left( \frac{m \times radns}{A} \right)$. The line width of the FMR lines, $\Delta H$, calculated as the line width at half of the peak intensity are quite large and therefore the $H_{res}$ values are known to be no better than 7.9 kA/m and the $\Delta H$ values are known to be no better than 15 kA/m (Table IV). Indeed all $H_{res}$ values are very close to the FMR field value expected for spherical magnetite nanoparticles. For MF and MC MNPs, which are in a ferromagnetic state as it is known from the magnetic measurements, this position of the resonance field can be interpreted as an argument to claim their sphericity. At the same time in case of the

existence of strong superparamagnetic contributions the role of the demagnetizing fields becomes more complex because one should take into account the demagnetizing fields created by nearby nanoparticles in each particular geometry of the MNPs ensemble.

In all cases the line width was large. It was discussed earlier that rather high linewidths are due to the fact that the observed resonances are a ''convolution'' of several closely spaced lines caused by the deviations from stoichiemetry and strain distributions, etc.[16,25,31] In general, mixing carefully with talc in order to dilute causes a decrease in the line width due to the reduction of the interactions and narrowing of the distribution of the demagnetizing fields from nearby MNPs. It is especially lowered when the MNPs are separated by centrifuging, MC-1 and MF-1: a narrower size distribution causes a more uniform distribution of the demagnetizing fields. The inset of figure 16 also shows that EEP MNPs from cyclone and filter become very similar after mixing with talc causing a narrower line width.

Comparative analysis of the structural features, magnetic properties and microwave absorption of the EEW MNPs clearly indicates that we are dealing with an ensemble in which the ferromagnetic contributions come from the MNPs with a nearly spherical shape. Additional separation by centrifuging obtains the ensembles of superparamagnetic MNPs of magnetite with a smaller size and a narrower size distribution. Although the primary magnetization curve analysis results are inappropriate for the evaluation of the shape of such a small nanoparticles, the microwave measurements still indicate that the MNPs keep their nearly spherical shapes ($\omega/\gamma \approx 240$ kA/m).

## IV. CONCLUSIONS

Electric explosion of iron wire in nitrogen/oxygen atmosphere was employed to produce two fractions of iron oxide air-dry spherical nanoparticles with number-average diameter 22 and 12 nm (according to TEM). XRD indicated that the major crystalline phase was magnetite (of about 90 to 95%) depending on the fraction. Further fractioning of air-dry EEW powders was performed in aqueous suspensions. Based on zeta-potential measurements the optimum concentration of electrostatic stabilizer, sodium citrate, and optimum pH level were found to provide the stability of EEW magnetite suspension in water. It was shown that stable suspension still contained the substantial fraction of aggregates, which can be disintegrated only by the excessive ultrasound treatment. The de-aggregation process was monitored by the dynamic light scattering. The separation of large particles from the suspension was performed by centrifuging. Additional separation of the ensemble by centrifuging obtained ensembles with a smaller size and a narrower size distribution, bringing the average MNP size below 10 nm. Maximum obtained concentration was as high as 5 % of magnetic material (by weight).

The structural features, magnetic properties and microwave absorption of the iron oxide magnetic nanoparticles fabricated by EEW clearly indicate that we are dealing with an ensemble in which the ferromagnetic contributions comes from the spherical MNPs. Despite the presence of magnetic interactions between the MNPs in fractionated samples, they showed similar behaviour to that expected of superparamagnetic ensembles. Designed assembly of de-aggregated nanoparticles is an example of on-purpose developed magnetic nanofluid.

[1] Y.-W. Jun, J.-W. Seo, and J. Cheon, Acc. Chem. Res. **41**, 179 (2008).
[2] L. R. Bickford, Phys. Rev. **78**, 449 (1950).
[3] Q. A. Pankhurst, J. Connolly, S. K. Jones, and J. Dobson, J. Phys. D: Appl. Phys. **36**, R167 (2003).

[4] G. V. Kurlyandskaya, S. M. Bhagat, S. E. Jacobo, J. C. Aphesteguy, and N. N. Schegoleva, J. Phys. Chem. Sol. **72**, 276 (2011).

[5] M. Jeun, S. Lee, J. K. Kang, A. T. Tomitaka, K. W. Kang, Y. I. Kim, Y. Takemura, K.-W. Chung, J. Kwak, and S. Bae, Appl. Phys. Lett. **100**, 092406 (2012).

[6] S. Guo, D. Li, L. Zhang, J. Li, and E. Wang, Biomaterials **30**, 1881 (2009).

[7] R. Hao, R. Xing, Z. Xu, Y. Hou, S. Gao, and S. Sun, Adv. Mater. **22**, 2729 (2010).

[8] A. G. Roca, D. Carmona, N. Miguel-Sancho, O. Bomati-Miguel, F. Balas, C. Piquer, and J. Santamaría, Nanotechnology **23**, 155603 (2012).

[9] J. Llandro, J. J. Palfreyman, A. Ionescu, and C. H. W. Barnes, Med. Biol. Eng. Comput. **48**, 977 (2010).

[10] J. T. Mayo, C. Yavuz, S. Yean, L. Cong, H. Shipley, W. Yu, J. Falkner, A. Kan, M. Tomson, and V. L. Colvin, Sci. Technol. Adv. Mater. **8**, 71 (2007).

[11] R. Fan, X. H. Chen, and Z. Gui, Mater. Res. Bull. **36**, 497 (2001).

[12] D. E. Zhang, Z. W. Tong, S. Z. Li, X. B. Zhang, and A. L. Ying, Mater Lett **62**, 4053 (2008).

[13] A. G. Roca, R. Costo, A. F. Rebolledo, S. Veintemillas-Verdaguer, P. Tartaj, T. Gonzalez-Carreno, M. P. Morales, and C. J. Serna, J. Phys. D: Appl. Phys. **42**, 224002 (2009).

[14] S. Sun, H. Zeng, D. B. Robinson, S. Raoux, M. Rice, S. X. Wang, and G. Li, J. Am. Chem. Soc. **126**, 273 (2004).

[15] A. Kumar, S. Mohapatra, V. Fal-Miyar, A. Cerdeira A, J. A. García, H. Srikanth, J. Gass, and G. V. Kurlyandskaya, Appl. Phys. Lett. **91**, 143902 (2007).

[16] G. V. Kurlyandskaya, J. Cunanan, S. M. Bhagat, J. C. Aphesteguy, and S. E. Jacobo, J. Phys. Chem. Sol. **68**, 1527 (2007).

[17] L. Néel, Ann. Geophys. **5**, 99 (1949).

[18] W. F. Brown Jr., Phys. Rev. **130**, 1677 (1963).

[19] V. A. Ignatchenko, I. S. Edelman, and D. A. Petrov, Phys. Rev. B **81** 054419 (2010).

[20] D. G. Chen, X. G. Tang, J. B. Wu, W. Zhang, Q. X. Liu, and Y. P. Jiang, J. Magn. Magn. Mater. **323**, 1717 (2011).

[21] L. Q. Yu, L. J. Zheng, and J. X. Yang, Mater. Chem. Phys. **66**, 6 (2000).

[22] Y. B. Khollam, S. R. Dhage, and S. B. Potdar, Mater Lett **56**, 571 (2002).

[23] T. Matsunaga, K. Maruyama, T. Takeyama, and T. Katoh, Bios. Bioelectr. **22**, 2315 (2007).

[24] Yu. A. Kotov, J. Nanoparticle Res. **5**, 539 (2003).

[25] G. V. Kurlyandskaya, S. M. Bhagat, A. P. Safronov, I. V. Beketov, and A. Larrañaga, AIP Advances **1**, 042122 (2011).

[26] Yu. A. Kotov, E. I. Azarkevich, I. V. Beketov, T. M. Demina, A. M., Murzakaev, and O. M., Samatov, Key Eng. Mater. **132-136**, 173 (1997).

[27] A. M. Murzakaev, V. L. Kuznetsov, O. M. Samatov, T. M. Demina, O. R. Timoshenkova, and A. K. Shtoltz, Inorganic materials **43**, 633 (2007).

[28] H. M. Rietveld, Appl. Crystallogr. **2**, 65 (1969).

[29] P. Scherrer, Nachr Ges Wiss Göttingen **26**, 98 (1918).

[30] J. S. Ramachandran, S. M. Bhagat, and J. L. Peng, Solid State Commun. **96**, 127 (1995).

[31] G. V. Kurlyandskaya, S. M. Bhagat, C. Luna, M. Vazquez, J. Appl. Phys. **99**, 104308 (2006).

[32] Y. Zhang, Y. Chen, P. Westerhoff, K. Hristovski, and J. C. Crittenden, Water Res. **42**, 2204 (2008).

[33] Y. Hwang, J.-K. Lee, Y.-M. Jeong, S. Cheong, Y.-Ch. Ahn, and S. H. Kim, Powder Technology **186**, 145 (2008).

[34] S. J. Chung, J. P. Leonard, I. Nettleship, J. K. Lee, Y. Soong, D. V. Martello, and M. K. Chyu, Powder Technology **194**, 75 (2009).

[35] A. W. Pacek, P. Ding, and A. T. Utomo, Powder Technology **173**, 203 (2007).

[36] P. C. Hidber, T. J. Graule, and, L. J. Gauckler, J. Am. Ceram. Soc. **79**, 1857 (1996).

[37] P. C. Hiemenz and R. Rajagopalan, *Principles of Colloid and Surface Chemistry* (Marcel Dekker, New York, 1997) p. 499.

[38] M. Kosmulski, *Chemical properties of material surfaces* (Marcel Dekker, New York, Basel, 2001) p. 248.

[39] W. W. Tscharnuter, in *Encyclopedia of Analytical Chemistry*, Ed. by R. A. Meyers (John Wiley & Sons Ltd., 2001) p. 5469.

[40] E. W. J. Verwey, Nature **144**, 327 (1939)

[41] J. S. Salazar, L. Perez, O. de Abril, L. T. Phuoc, D. Ihiawakrim, M. Vazquez, J.-M. Greneche, S. Begin-Colin, and G. Pourroy, Chem. Mater. **23**, 1379 (2011).

[42] G. F. Goya, T. S. Berquó, F. C. Fonseca, and M. P. Morales, J. Appl. Phys. **94**, 3520 (2003).

[43] R. W. Chantrell and E. P. Wohlfarth, Phys. Stat. Sol. A **91**, 619 (1985).

[44] E. P. Wohlfarth, Phys. Lett. A **70**, 489 (1979).

[45] R. C. O´Handley, *Modern Magnetic Materials* (John Wiley & Sons, New York, USA, 1972) p. 740.

[46] S. Morup, C. Frandsen, and M. F. Hansen, Beilstein J. Nanotechnol. **1**, 48 (2010).

[47] B. D. Cullity, *Introduction to Magnetic Materials* (Addison-Wesley, Reading, MA, USA, 1972) p 544.

[48] V. V. Srinivasu, S. E. Lofland, S. M. Bhagat, K. Ghosh, and S. D. Tyagi, J. Appl. Phys. **86**, 1067 (1999).

[49] F. J. Owens, J. Phys. Chem. Solids **64**, 2289 (2003).